Nano Research

ISSN 1998-0124 CN 11-5974/O4
https://doi.org/10.1007/s12274-020-3158-1

Research Article

Superhydrophobic, photo-sterilize, and reusable mask based on graphene nanosheet-embedded carbon (GNEC) film

Zezhou Lin[1], Zheng Wang[2], Xi Zhang[1] (✉), and Dongfeng Diao[1]

[1] *Institute of Nanosurface Science and Engineering, Guangdong Provincial Key Laboratory of Micro/Nano Optomechatronics Engineering, Shenzhen University, Shenzhen 518060, China*
[2] *Shenzhen Anhio Medical Technology Co., Ltd, Shenzhen 518110, China*

Received: 21 August 2020 / **Revised:** 29 September 2020 / **Accepted:** 4 October 2020

ABSTRACT

The 2019 coronavirus disease (COVID-19) has affected more than 200 countries. Wearing masks can effectively cut off the virus spreading route since the coronavirus is mainly spreading by respiratory droplets. However, the common surgical masks cannot be reused, resulting in the increasing economic and resource consumption around the world. Herein, we report a superhydrophobic, photo-sterilize, and reusable mask based on graphene nanosheet-embedded carbon (GNEC) film, with high-density edges of standing structured graphene nanosheets. The GNEC mask exhibits an excellent hydrophobic ability (water contact angle: 157.9°) and an outstanding filtration efficiency with 100% bacterial filtration efficiency (BFE). In addition, the GNEC mask shows the prominent photo-sterilize performance, heating up to 110 °C quickly under the solar illumination. These high performances may facilitate the combat against the COVID-19 outbreaks, while the reusable masks help reducing the economic and resource consumption.

KEYWORDS

COVID-19, graphene nanosheet, superhydrophobic, photo-sterilize

1 Introduction

Coronavirus disease 2019 (COVID-19) has spread to more than 200 countries and regions [1, 2]. By 27th September 2020, the number of confirmed cases has surpassed 32,730,945 worldwide with 991,224 deaths, according to data compiled by World Health Organization (WHO) [3]. Coronavirus spread through direct or indirect contact, respiratory droplets (including larger droplets that fall rapidly near the source as well as coarse aerosols with aerodynamic diameter > 5 μm), and fine-particle aerosols (diameter ≤ 5 μm) [4, 5]. Coronavirus is highly contagious and can be transmitted through respiratory droplets and contact with infected persons or fomites [6]. Droplet refers to the saliva and snot from the ill individuals talking, coughing, or sneezing. Surgical face masks could prevent transmission of human coronaviruses and influenza viruses from symptomatic individuals [7–9]. Nevertheless, the current surgical face masks still have some limitations [10–12]. Firstly, although the common mask filters the main dust particles (> 10 μm), the bacteria and virus filtration efficiency still need to be improved. Secondly, the lack of superhydrophobic properties caused the droplets (carrying virus) remain on the surface. Thirdly, the mask without photo- sterilize cannot be used for a long time or repeatedly, since the absorbed viruses might survive on their surfaces. Shortage of face masks is a current critical concern since the emergence of pandemic [13]. The increasing demand for masks, the large number of raw materials consumed in the preparation, and the disposal of a large number of discarded masks are all issues of great concern.

Coronavirus can hardly be transmitted by itself and requires respiratory droplets as the virus carrier [8]. Surgical masks could block the droplets containing the virus by reducing the amount and speed of droplets, and prevent the wearer from breathing in them. The peculiar properties of superhydrophobic coatings (water contact angle > 150°) [14], such as self-cleaning, anti-bacteria, and so on, are the most dramatic [15, 16]. During recent research, microstructures have accelerated the progress of the superhydrophobic surfaces. Common polymers, such as polystyrene, polyethylene, polypropylene [17–19], heterogeneous graphene [20], and nano-hierarchical structures [21], have been prepared as superhydrophobic and anti-virus coatings. Nevertheless, reports on surgical masks with superhydrophobic ability are still rare.

Here, we reported a superhydrophobic, photo-sterilize, and reusable mask that can be worn for a long time and reused after solar illumination. The mask is based on graphene nanosheet-embedded carbon (GNEC) film and developed by ultrasonic-extrusion, to provide protection against the COVID-19. In hydrophobicity and photothermal properties, GNEC masks show better performance (water contact angle: 157.9°, temperature: 110 °C) than laser-induced graphene (silver nanoparticles) coatings (water contact angle: 140°, temperature: ~ 90 °C) [22].

2 Results and discussion

Superhydrophobic surfaces for surgical masks can be realized by using the ultrasonic extrusion method to embed GNEC

Address correspondence to zh0005xi@szu.edu.cn

nanostructure in smooth fibers (polypropylene, chemical structural formula: $-[CH_2-CH(CH)_3]_n-$). As shown in Fig. 1(a), the GNEC films were deposited on Si substrate by using electron cyclotron resonance (ECR) sputtering system (see Fig. S1 and Experimental Section in the Electronic Supplementary Material (ESM) for details). Low energy electrons exchange energy with valence electrons of carbon atoms through inelastic scattering, and induce the change of C–C hybridization mode from sp^3 to sp^2. During one inelastic scattering process of irradiating electron, its kinetic energy is lost through several means (electron excitation, plasmon excitation, phonon excitation, etc.). When the energy loss is large enough, one part of it ΔE can trigger the hybridization change of carbon atom by breaking a C–C bond in sp^3 system. This increasing electron energy loss is essential for breaking the C–C bond to form sp^2 hybridization. With the assistant of the low-energy electrons, a large number of graphene nanosheets (GNs) embedded in amorphous carbon grow vertically to the substrate. Due to the large number of standing-structured GNs embedded in the film, the density of graphene edges is considerably high. The electron energy was modulated by deposited voltage (V_{dep}) which affects the size and number of GNs. The detailed information of ECR apparatus and depositing process could be found in our former work [23–25]. The cross-sectional sample of 40 V GNEC film on the substrate was prepared by focused ion beam (FIB) etching (see Fig. S2 in the ESM for details). From the transmission electron microscope (TEM) image of the cross-sectional sample, GNs grew vertically on silicon substrate with the vertical thickness of 70 nm. Based on a lot of our previous research, the high edge density of graphene nanosheet was fabricated by setting the substrate bias 40 V (see Fig. S3 in the ESM for details).

Figure 1(b) illustrates the fabrication process of GNEC mask by the ultrasonic extrusion method. Specifically, the thicknesses of GNEC film is 70 nm controlled by the deposited time, the inset shows that the graphene nanosheets grew vertically on the Si substrate. Electric carving device with 11,000 min^{-1} high-frequency varication was used for exfoliating the GNEC film from the Si substrate. Before processing, 10 mL of alcohol was used for wiping the surface of GNEC/Si substrate for 10 s to remove the dust particles. The clamp (with rubber head) was used for fixing the GNEC/Si substrate. When the carving device power is stabilized at 50 W, the substrate vibrates evenly to peel off the GNEC film fragments. The collected GNEC fragment was uniformly and randomly distributed on the melt-blown fibers (area: 17.2 cm × 9.2 cm), which are made of thermoplastics such as polypropylene [26]. A handful of silicon doped graphene may provide a considerably carrier mobility [27]. The ultrasonic extrusion platform was used to embed GNEC nanostructure in smooth fibers. The extrusion time is 10 s with the ultrasonic frequency of 40 kHz and the working power of 600 W (see Fig. S4 in the ESM for details). Unlike the smooth fibers of pristine surgical mask, the fibers of new mask were covered by GNEC film fragments randomly and evenly. During the ultrasonic extrusion process, the graphene nanosheets are not required to grow vertically to the fiber, since the GNEC film fragment has already contained a high density of graphene edges due to its unique nanostructure.

Figure 2(a) shows the principle of hydrophobicity caused by electron trapping at edges of GNs. The repulsive force between GNEC film and water droplet was enhanced by the surface charges. The edge quantum wells serve as electron trapping centers. In the Hubbard model, the spin-polarized Hamiltonian of graphene p_z electron can be expressed as [28]:

$$H_\sigma = \sum_{i,\sigma} \Delta_i c_{i,\sigma}^{+} c_{i,\sigma} + \sum_{<i,j>,\sigma} t_{ij}(f_{ij} c_{i,\sigma}^{+} c_{j,\sigma} + f_{ij}^{*} c_{j,\sigma}^{+} c_{i,\sigma}) + \sum_i U_i \hat{n}_{i,\sigma} \hat{n}_{i,-\sigma}$$

$$t_{ij} = < i \mid V_i \mid j > \quad (1)$$

where i represents the i-th atom, j represents the nearest neighbor, σ is the spin with sign, t_{ij} is the overlap integral between the nearest neighbors, f_{ij} is the periodic factor determined by the structure, $c_{i,\sigma}^{+}$ and $c_{i,\sigma}$ are the creation and annihilation operator in Wannier representation, and $n_{i,\sigma} = c_{i,\sigma}^{+} c_{i,\sigma}$ represents the

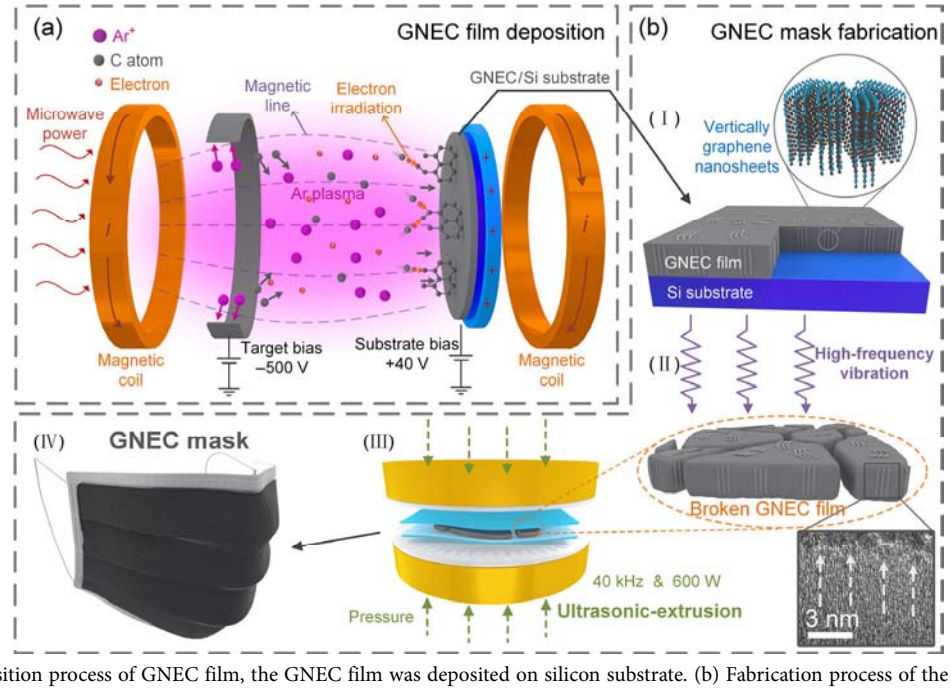

Figure 1 (a) Deposition process of GNEC film, the GNEC film was deposited on silicon substrate. (b) Fabrication process of the GNEC mask. (I) The deposited GNEC film with vertically grown graphene nanosheets with the thickness of 70 nm. (II) GNEC film was broken by high-frequency vibration. (III) Ultrasonic-extrusion of GNEC film with 40 kHz and 600 W, the GNEC fragment was uniformly distributed between the melt-blown fibers. (IV) A three-dimensional diagram of the finished GNEC mask.

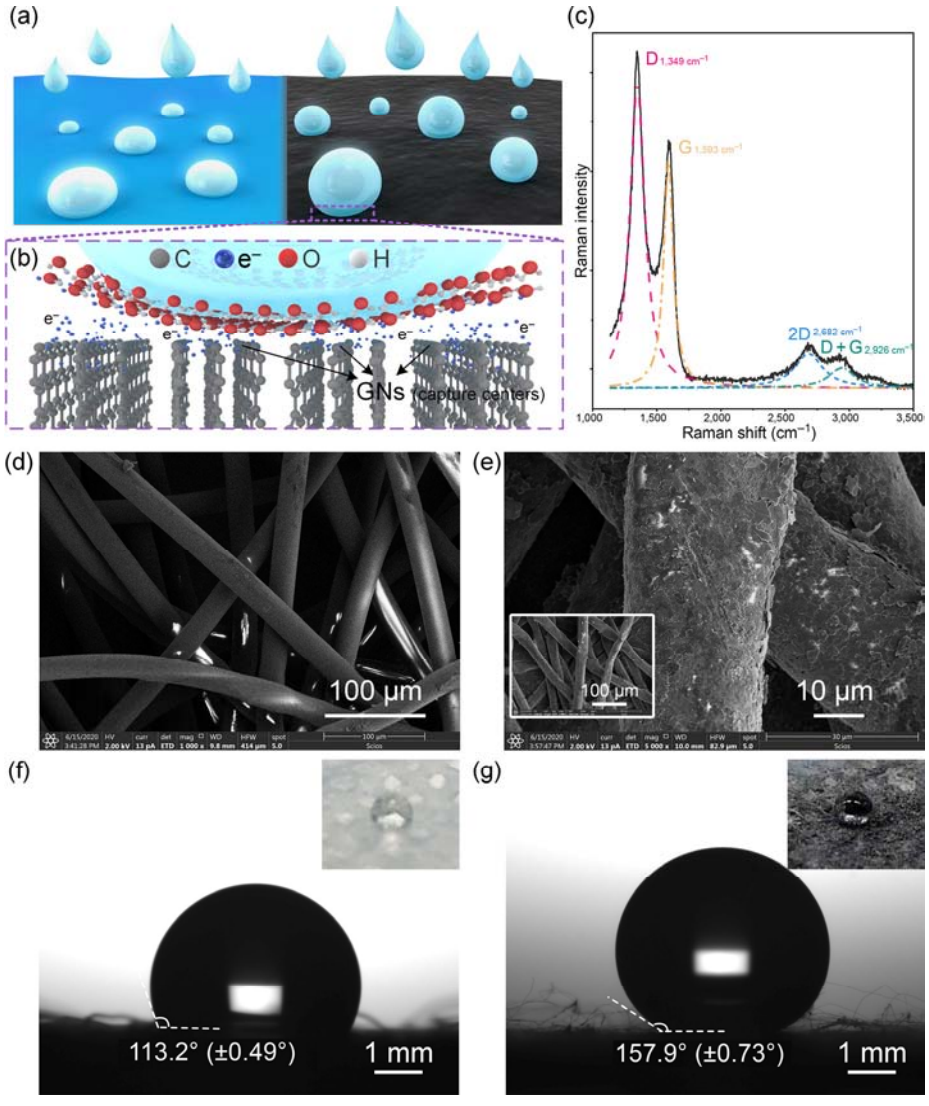

Figure 2 (a) Schematic illustration of the surface of pristine mask and GNEC mask. (b) Intrinsic mechanism of the superhydrophobic property of GNEC mask. (c) Raman spectrum of the GNEC mask. SEM of the smooth fiber of pristine mask (d) and the graphene nanosheets embed nonwoven fiber within the GNEC mask (e), the inset is a zoom-out image. Water contact angle measurement of pristine mask (f) and GNEC mask (g), with a volume of 5 μL water.

particle-number operator. The diagonal energy Δ_i is the onsite integral. U_i is the Hubbard repulsive energy. V_i is the effective atomic potential.

At edges, the effective coordination number decreases, and the Hamilton matrix can be corrected as

$$\begin{cases} C_z(z) = d_i(z_i)/d_{iB} & \text{(Bond contraction)} \\ C_z^{-m} = \dfrac{E_i(z_i)}{E_{iB}} = \dfrac{V(z_i)}{V_B} & \text{(Bond energy; potential)} \\ \dfrac{t(z_i)}{t_B} = \dfrac{<\phi_i(r)\,|\,V_i(z_i)\,|\,\phi_i(r)>}{<\phi_i(r)\,|\,V_{iB}\,|\,\phi_i(r)>} \cong \\ \qquad \dfrac{V_i(z_i)}{V_{iB}} \cong C_z^{-m} & \text{(Hopping integral)} \\ U_i(z_i)/U_j(z_j) = [C_z(z_i)/C_z(z_j)]^{-3} & \text{(Repulsion energy)} \end{cases} \tag{2}$$

where the effective coordination number (z), bond length (d), the indicator for bond nature of carbon (m), the wave function ($\phi_i(r)$), bond contraction coefficient (C_z), single bond energy (E), atomic potential (V_i), Hamiltonian integrals t, and Hubbard U were taken into consideration. The modification of under-coordinated is with respect to the bulk values (B).

At the edge of GN, bond length (d_i) was shortened by C_z compared with that of bulk (d_0) due to the automatically relaxation towards lower energy [29]. Equation (2) indicated that the effective atomic potential (V_i) to neighbor electrons at the edges was lowered (by C_z^{-m}) compared with those in bulk, which tends to trap the excess electrons [29, 30] and unpaired spins [29, 31]. In GNEC film, a large number of standing structured GNs provide high density of edges and trapped electrons. The surface aggregated charges of GNEC film make the mask hydrophobic.

The microstructural and physical properties of the GNEC mask are systematically characterized. In the Raman spectrum of the GNEC film, the D peak, the G peak, and the 2D peak were used to characterize the structural defects and edges, the number of layers of the GN, and the stacking pattern of the graphene layer. The ratio of the D peak/G peak I_D/I_G is used to indicate the edge structure of the GNEC film, and the 2D peak is used to indicate the crystallinity of the GNEC film [32]. The nanostructures of graphene nanosheet have been verified by Raman spectra in Fig. 2(c). A strong 2D peak around 2,682 cm^{-1} appears and the I_D/I_G is 1.38, indicating the formation of small-size graphene nanosheets embed in the smooth fibers.

As shown in Fig. 2(d), scanning electron microscopy (SEM) was used for observing the micro-structures of pristine mask.

The nonwoven polymer, is composed of melt-blown fibers (diameter: 25 μm), which are distributed randomly and cross each other. Figure 2(e) displays SEM images of GNEC mask after ultrasonic-extrusion. Unlike the smooth fibers of pristine surgical mask, GNEC mask was randomly and evenly covered with graphene nanosheets nanostructure. Ultrasonic extrusion process and the optical image of the pristine mask and GNEC mask were shown in Fig. S5 in the ESM. Details of equipment and setting used for water contact angle can be found in the Experimental Section in the ESM. Coronavirus can hardly be transmitted by itself and requires respiratory droplets as the virus carrier. As shown in Fig. 2(f), a static water contact angle was used for investigating the wetting state of the pristine mask. The contact angle of 5 μL water on the pristine mask surface is about 113.2° (±0.49°), which is the average of the three locations of the same mask and each location was measured 30 times (measuring time: 15 s, frequency: 2 Hz). Multiple measurements show the weak hydrophobic property of pristine mask, resulting from the surface of the nonwoven polymer, is smooth and lacks nanostructures. Although weak hydrophobic properties are possessed, virus droplets still probably adhere to the surface of the pristine mask. After ultrasonic-extrusion, graphene nanosheets embedded nano-structures on the surface of the fibers improving the hydrophobic properties. Superhydrophobic properties reduce the amount of droplets adsorption facilitating medical application. The surface chemistry, material molecular weight, and structure are important in this case, especially the polarity of any defect groups. In the case of graphene-based surfaces, the defects will be key determinants of the hydrophobicity and hydrophilicity [28, 33]. As shown in Fig. 2(g), the GNEC mask exhibits excellent superhydrophobic performance, wherein the maximum contact angles of the GNEC mask can reach to 157.9° (±0.73°). The super-hydrophobicity may arise from the repulsive force between GNEC film and water droplet enhanced by the surface charges trapped by edges. Superhydrophobic surface effectively prevents the respiratory droplets (containing virus) from attaching to the mask.

Generally, self-cleaning materials are cleared by rolling water droplets to keep the surface clean [34, 35]. The rolling angle of GNEC mask is also measured as we investigate the movement of droplets on a mask that people wear daily. Figure S6 in the ESM shows the water rolling process of the GNEC mask, the tilt angle of the test platform is 0° – 90° (tilt speed: 0.5°/s). At a small inclined angle (7.0°) of the platform, the droplets perceptibly roll on the mask surface. As the angle continues to increase to 45°, the test drop rolled out of the measured range, indicating excellent rolling characteristics. During the daily use of masks, which should be fitted to the wearer's face instead of parallel to the ground, all places of the mask have a large inclined angle (about 90° ± 30°), which meets the rolling condition (> 7.0°) of GNEC mask. The result indicates the potential medical application in daily life that the infected droplet (containing virus) that meets the mask will roll and slide over the surface of mask (about 60° – 120°) because the GNEC mask possesses the small rolling angle (7.0°), indicating the lower appearance of remaining droplets.

Filter efficiency measurement is a crucial step before surgical masks are commercially available. Respiratory droplets exist in different sizes, where aerosols specifically consist of droplets that are sub-5 μm in size. Droplets that are larger than 5 μm generally do not spread long distances and settle within 1–2 m as a result of gravity sedimentation [36]. Masks that meet specific testing requirements can only be used for people. Bacterial Filtration Efficiency (BFE) is a common and major test item, which refers to the filtration efficiency of aerosols (diameter: 2.5 μm). In high-risk situations, mask requires more stringent measuring standards. Particulate Filtration Efficiency (PFE) is used for measuring non-oily suspended particles (0.3 μm). As for the surgical mask, Technical Standard of Surgical Masks (Y0469-2011) is common measuring standard with BFE > 95% and PFE > 30%.

Figure 3(a) illustrates the experimental apparatus of filter efficiency measurement. Sodium chloride (NaCl) aerosol is often used in mask filtration efficiency measurement [37]. The NaCl aerosols are generated by the aerosol generator, producing particles (0.1 – 10 μm). The air flow rate (88.1 L/min) is measured using a hot wire anemometer and the resistance (884.0 Pa) is measured using a digital manometer. To prevent the experimental error caused by the movement, the prepared mask is held in place using the clamp for a better seal. The effective area of the mask sample during the tests was ~ 100 cm^2. The particle analyzer collects the passing particles and analyses the filter efficiency of different diameters particles (10, 5, 2.5, 1, 0.5, and 0.3 μm), respectively. As shown in Fig. 3(b), the pristine mask filtered 95.43% of the 2.5 μm particles (BFE) and 34.68% of the 0.3 μm particles (PFE), meeting the Y0469-2011 standards. In contrast, the GNEC mask exhibits the outstanding filter efficiency (BFE = 100% and PFE = 94.01%). Compared with Figs. 2(c) and 2(e), there are large holes in the inter-crossing fibers. Pristine masks can block most particles over 2.5 μm. Due to the existence of holes, particles between

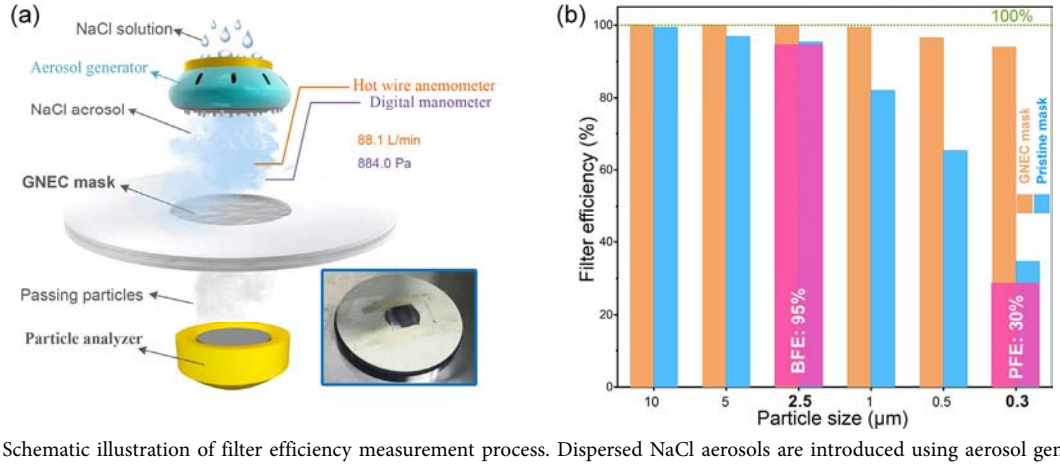

Figure 3 (a) Schematic illustration of filter efficiency measurement process. Dispersed NaCl aerosols are introduced using aerosol generator, passing through the measured mask. The passing aerosols are analyzed using particle analyzers, and the filter efficiencies are determined by collected particle concentrations. The inset shows the clamp and the testing process. (b) Mask filtration efficiency measurement. The blue represents the pristine mask and the orange represents the GNEC mask. The pink represents Technical Standard of Surgical Masks (Y0469-2011), BFE > 95% and PFE > 30%.

0.3 and 2.5 μm readily pass through the nonwoven fabric resulting in the low PFE. After ultrasonic extrusion, the graphene nanosheets are firmly embedded into the nanosheets filling the holes. We speculate that the enhanced performance of the hybrids is likely due to the combined effect of mechanical and trapped electron-based filtration. With the assistance of high-density graphene nanosheets, even small particles of 0.3 μm are difficult to pass through the GNEC mask. The enhancement of filtration efficiency may origin from the change of microstructure of fibers caused by adding GNEC films, and can be attributed to the surface electrons trapping of GNEC film.

To further study the GNEC mask to sterilize the residual virus, the photothermal performances were investigated on the surface. Coronaviruses have a protein "ridge" (spike protein) that binds to human cells more strongly than similar viruses, enabling them to better infect and spread faster [38]. Spike proteins are sensitive to temperature, which can be inactivated by high temperatures. Recent studies have shown that under heating at 56 °C for 30 minutes, coronavirus cannot be killed completely and researchers have found that the virus can still replicate. The thermal performance of the mask was studied by measuring the surface temperature under simulated lighting conditions with the infrared camera. As shown in Figs. 4(a) and 4(b), the infrared camera was used to measure the temperature distribution on the surface of pristine mask and GNEC mask, under the 1,769 W/m^2 solar illumination (at 21 V input voltage) in 200 s. As shown in Fig. 4(c), the temperature of the mask stabilized around 40 °C after 200 s of solar illumination (at 21 V input voltage), which is useless for disinfection. In contrast, the temperature of GNEC mask surface rapidly rises to 87 °C (±16.1 °C) in 20 s and stabilizes to 105 °C (±8.4 °C) in 50 s. Most viruses are inactivated over 80 °C, and the photo-sterilize GNEC mask can be spontaneously performed under short-time solar illumination. Additionally, under normal and mild natural light, it does not sterilize itself, so there is not worry about the wearers, which will hurt their faces. Figure 4(d) shows the optical absorption spectrum of pristine and GNEC masks. In the visible to the near infrared region (400 – 1,100 nm), pristine mask has low optical absorption with 45% – 60%. However, the ultrasonic extruded GNEC mask showed outstanding spectral absorption performance (greater than 99.5%) in the same range. The high absorption is beneficial for GNEC masks to show stronger photothermal performance. Compared to pristine mask, GNEC mask possesses the photo-sterilize capacity, wiping out the viruses in a short time and making the mask reusable. After 24, 48, and 72 h solar illumination (1,262 W/m^2), repeated experiments were conducted on the superhydrophobic and photothermal properties (at 15 V input voltage) of GNEC masks to determine reusability. The results of the water contact angle test (Fig. S7 in the ESM) and the surface temperature measurement (Fig. S8 in the ESM) kept their advanced performances in the superhydrophobic and photothermal features, indicating the feasibility of applications from the reused masks. Furthermore, mental clusters play an important role in anti-virus effects [39]. In further studies, we will consider doping metal cluster to achieve better performance.

3 Conclusions

Hence, we have reported a superhydrophobic, photo-sterilize, and reusable mask based on GNEC film, thus potentially contributing to control the rapid spread of the COVID-19. GNEC films were deposited by ECR sputtering system, containing a large number of standing structured GNs. The ultrasonic extrusion method was used for fabricating the GNEC mask. GNEC mask exhibits excellent properties, including superhydrophobic (water contact angle: 157.9°), ultrahigh bacterial filtration efficiency (BFE: 100%), and photo-sterilize (photothermal performance: 110.6 °C). People may be inspired by this work to explore the better performance of surgical masks, together to maintain global health and development.

Acknowledgements

This work was supported by the National Natural Science Foundation of China (No. 51605306) and Shenzhen Overseas High-Level Talents Innovation and Entrepreneurship Plan

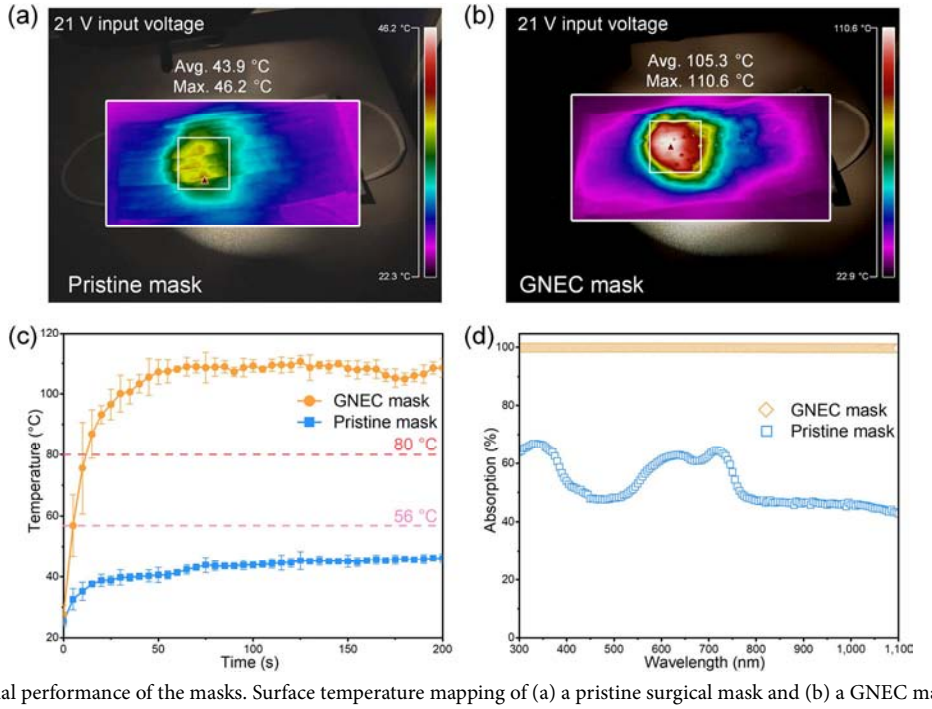

Figure 4 Photothermal performance of the masks. Surface temperature mapping of (a) a pristine surgical mask and (b) a GNEC mask after 200 s of solar illumination (at 21V input voltage). (c) Surface temperature measurement for pristine surgical masks and GNEC masks. (d) Optical absorption of pristine and GNEC masks.

(No. KQJSCX20180328094853770). The authors would like to thank the Electron Microscopy Center (EMC) of Shenzhen University for their technical supports in TEM and FIB.

Electronic Supplementary Material: Supplementary material (further details of electron cyclotron resonance (ECR) sputtering system, deposition of GNEC film, fabrication of GNEC mask, and characterization of the GNEC mask) is available in the online version of this article at https://doi.org/10.1007/s12274-020-3158-1.

References

[1] Andersen, K. G.; Rambaut, A.; Lipkin, W. I.; Holmes, E. C.; Garry, R. F. The proximal origin of SARS-CoV-2. *Nat. Med.* **2020**, *26*, 450–452.

[2] Wang, H. W.; Wang, Z. Z.; Dong, Y. Q.; Chang, R. J.; Xu, C.; Yu, X. Y.; Zhang, S. X.; Tsamlag, L.; Shang, M. L.; Huang, J. Y. et al. Phase-adjusted estimation of the number of Coronavirus Disease 2019 cases in Wuhan, China. *Cell Discov.* **2020**, *6*, 10.

[3] WHO. *Coronavirus disease (COVID-19)*[Online]. https://www.who.int/docs/default-source/coronaviruse/situation-reports/20200928-weekly-epi-update.pdf?sfvrsn=9e354665_2.

[4] Zou, L. R.; Ruan, F.; Huang, M. X.; Liang, L. J.; Huang, H. T.; Hong, Z. S.; Yu, J. X.; Kang, M.; Song, Y. C.; Xia, J. Y. et al. SARS-CoV-2 viral load in upper respiratory specimens of infected patients. *New Engl. J. Med.* **2020**, *382*, 1177–1179.

[5] Peiris, J. S. M.; Lai, S. T.; Poon, L. L. M.; Guan, Y.; Yam, L. Y. C.; Lim, W.; Nicholls, J.; Yee, W. K. S.; Yan, W. W.; Cheung, M. T. et al. Coronavirus as a possible cause of severe acute respiratory syndrome. *Lancet* **2003**, *361*, 1319–1325.

[6] Karimi, S.; Arabi, A.; Shahraki, T.; Safi, S. Detection of severe acute respiratory syndrome Coronavirus-2 in the tears of patients with Coronavirus disease 2019. *Eye* **2020**, *34*, 1220–1223.

[7] Leung, C. C.; Lam, T. H.; Cheng, K. K. Mass masking in the COVID-19 epidemic: People need guidance. *Lancet* **2020**, *395*, 945.

[8] Leung, N. H. L.; Chu, D. K. W.; Shiu, E. Y. C.; Chan, K. H.; McDevitt, J. J.; Hau, B. J. P.; Yen, H. L.; Li, Y.; Ip, D. K. M.; Peiris, J. S. M. et al. Respiratory virus shedding in exhaled breath and efficacy of face masks. *Nat. Med.* **2020**, *26*, 676–680.

[9] El-Atab, N.; Qaiser, N.; Badghaish, H.; Shaikh, S. F.; Hussain, M. M. Flexible nanoporous template for the design and development of reusable Anti-COVID-19 hydrophobic face masks. *ACS Nano* **2020**, *14*, 7659–7665.

[10] Majchrzycka, K.; Okrasa, M.; Szulc, J.; Jachowicz, A.; Gutarowska, B. Survival of microorganisms on nonwovens used for the construction of filtering facepiece respirators. *Int. J. Environ. Res. Public Health* **2019**, *16*, 1154.

[11] Konda, A.; Prakash, A.; Moss, G. A.; Schmoldt, M.; Grant, G. D.; Guha, S. Aerosol filtration efficiency of common fabrics used in respiratory cloth masks. *ACS Nano* **2020**, *14*, 6339–6347.

[12] Zhong, H.; Zhu, Z. R.; Lin, J.; Cheung, C. F.; Lu, V. L.; Yan, F.; Chan, C. Y.; Li, G. Reusable and recyclable graphene masks with outstanding superhydrophobic and photothermal performances. *ACS Nano* **2020**, *14*, 6213–6221.

[13] Ullah, S.; Ullah, A.; Lee, J.; Jeong, Y.; Hashmi, M.; Zhu, C. H.; Joo, K. I.; Cha, H. J.; Kim, I. S. Reusability comparison of melt-blown vs nanofiber face mask filters for use in the coronavirus pandemic. *ACS Appl. Nano Mat.* **2020**, *3*, 7231–7241.

[14] Marmur, A. Hydro- hygro- oleo- omni-phobic? Terminology of wettability classification. *Soft Matter* **2012**, *8*, 6867–6870.

[15] Zhu, H.; Guo, Z. G.; Liu, W. N. Adhesion behaviors on superhydrophobic surfaces. *Chem. Commun.* **2014**, *50*, 3900–3913.

[16] Song, L. J.; Sun, L. W.; Zhao, J.; Wang, X. H.; Yin, J. H.; Luan, S. F.; Ming, W. H. Synergistic superhydrophobic and photodynamic cotton textiles with remarkable antibacterial activities. *ACS Appl. Bio Mater.* **2019**, *2*, 2756–2765.

[17] Hong, D. J.; Ryu, I.; Kwon, H.; Lee, J. J.; Yim, S. Preparation of superhydrophobic, long-neck vase-like polymer surfaces. *Phys. Chem. Chem. Phys.* **2013**, *15*, 11862–11867.

[18] Huovinen, E.; Takkunen, L.; Korpela, T.; Suvanto, M.; Pakkanen, T. T.; Pakkanen, T. A. Mechanically robust superhydrophobic polymer surfaces based on protective micropillars. *Langmuir* **2014**, *30*, 1435–1443.

[19] Liu, M. L.; Luo, Y. F.; Jia, D. M. Polydimethylsiloxane-based superhydrophobic membranes: Fabrication, durability, repairability, and applications. *Polym. Chem.* **2020**, *11*, 2370–2380.

[20] Ding, G. M.; Jiao, W. C.; Wang, R. G.; Yan, M. L.; Chu, Z. M.; He, X. D. Superhydrophobic heterogeneous graphene networks with controllable adhesion behavior for detecting multiple underwater motions. *J. Mater. Chem. A* **2019**, *7*, 17766–17774.

[21] Si, Y. F.; Guo, Z. G. Superhydrophobic nanocoatings: From materials to fabrications and to applications. *Nanoscale* **2015**, *7*, 5922–5946.

[22] Zhong, H.; Zhu, Z. R.; You, P.; Lin, J.; Cheung, C. F.; Lu, V. L.; Yan, F.; Chan, C. Y.; Li, G. J. Plasmonic and Superhydrophobic Self-Decontaminating N95 Respirators. *ACS Nano* **2020**, *14*, 8846–8854.

[23] Zhang, X.; Lin, Z. Z.; Peng, D.; Ye, L.; Zang, J. F.; Diao, D. Edge-state-enhanced ultrahigh photoresponsivity of graphene nanosheet-embedded carbon film/silicon heterojunction. *Adv. Mater. Interfaces* **2019**, *6*, 1802062.

[24] Wang, C.; Zhang, X.; Diao, D. F. Nanosized graphene crystallite induced strong magnetism in pure carbon films. *Nanoscale* **2015**, *7*, 4475–4481.

[25] Zhang, X.; Peng, D.; Lin, Z. Z.; Chen, W. C.; Diao, D. F. Edge effect on the photodetection ability of the graphene nanocrystallites embedded carbon film coated on p-silicon. *Phys. Status Solidi RRL* **2019**, *13*, 1800511.

[26] Lee, Y.; Wadsworth, L. C. Structure and filtration properties of melt blown polypropylene webs. *Polymer Eng. Sci.* **1990**, *30*, 1413–1419.

[27] Wang, Z. G.; Li, P. J.; Chen, Y. F.; Liu, J. B.; Zhang, W. L.; Guo, Z.; Dong, M. D.; Li, Y. R. Synthesis, characterization and electrical properties of silicon-doped graphene films. *J. Mater. Chem. C* **2015**, *3*, 6301–6306.

[28] Zhang, X.; Nie, Y. G.; Zheng, W. T.; Kuo, J. L.; Sun, C. Q. Discriminative generation and hydrogen modulation of the Dirac-Fermi polarons at graphene edges and atomic vacancies. *Carbon* **2011**, *49*, 3615–3621.

[29] Zhang, X.; Wang, C.; Sun, C. Q.; Diao, D. F. Magnetism induced by excess electrons trapped at diamagnetic edge-quantum well in multi-layer graphene. *Appl. Phys. Lett.* **2014**, *105*, 042402.

[30] Enoki, T.; Kobayashi, Y.; Fukui, K. I. Electronic structures of graphene edges and nanographene. *Int. Rev. Phys. Chem.* **2007**, *26*, 609–645.

[31] Ding, D.; Dai, X. Z.; Wang, C.; Diao, D. F. Temperature dependent crossover between positive and negative magnetoresistance in graphene nanocrystallines embedded carbon film. *Carbon* **2020**, *163*, 19–25.

[32] Pimenta, M. A.; Dresselhaus, G.; Dresselhaus, M. S.; Cançado, L. G.; Jorio, A.; Saito, R. Studying disorder in graphite-based systems by Raman spectroscopy. *Phys. Chem. Chem. Phys.* **2007**, *9*, 1276–1291.

[33] Liu, X. J.; Zhang, X.; Bo, M. L.; Li, L.; Tian, H. W.; Nie, Y. G.; Sun, Y.; Xu, S. Q.; Wang, Y.; Zheng, W. T. et al. Coordination-resolved electron spectrometrics. *Chem. Rev.* **2015**, *115*, 6746–6810.

[34] Zhu, H.; Wu, L. Z.; Meng, X.; Wang, Y. G.; Huang, Y.; Lin, M. H.; Xia, F. An anti-UV superhydrophobic material with photocatalysis, self-cleaning, self-healing and oil/water separation functions. *Nanoscale* **2020**, *12*, 11455–11459.

[35] Verho, T.; Bower, C.; Andrew, P.; Franssila, S.; Ikkala, O.; Ras, R. H. A. Mechanically durable superhydrophobic surfaces. *Adv. Mater.* **2011**, *23*, 673–678.

[36] Morawska, L. Droplet fate in indoor environments, or can we prevent the spread of infection? *Indoor Air* **2006**, *16*, 335–347.

[37] Cho, H. W.; Yoon, C. S.; Lee, J. H.; Lee, S. J.; Viner, A.; Johnson, E. W. Comparison of pressure drop and filtration efficiency of particulate respirators using welding fumes and sodium chloride. *Ann. Occup. Hyg.* **2011**, *55*, 666–680.

[38] Li, F. Structure, function, and evolution of coronavirus spike proteins. *Ann. Rev. Virol.* **2016**, *3*, 237–261.

[39] Lazar, P.; Zhang, S.; Šafářová, K.; Li, Q.; Froning, J. P.; Granatier, J.; Hobza, P.; Zbořil, R.; Besenbacher, F.; Dong, M. D. et al. Quantification of the interaction forces between metals and graphene by quantum chemical calculations and dynamic force measurements under ambient conditions. *ACS Nano* **2013**, *7*, 1646–1651.

Table of contents

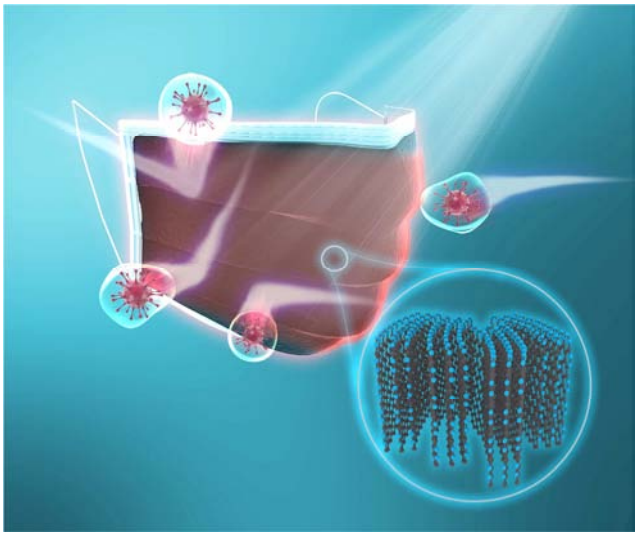

A superhydrophobic, photo-sterilize, and reusable mask based on graphene nanosheet-embedded carbon (GNEC) film was reported, with high-density edges of standing structured graphene nanosheets serving as electron trapping centers.

Electronic Supplementary Material

Superhydrophobic, photo-sterilize, and reusable mask based on graphene nanosheet-embedded carbon (GNEC) film

Zezhou Lin[1], Zheng Wang[2], Xi Zhang[1] (✉), and Dongfeng Diao[1]

[1] *Institute of Nanosurface Science and Engineering, Guangdong Provincial Key Laboratory of Micro/Nano Optomechatronics Engineering, Shenzhen University, Shenzhen 518060, China*
[2] *Shenzhen Anhio Medical Technology Co., Ltd, Shenzhen 518110, China*

Supporting information to https://doi.org/10.1007/s12274-020-3158-1

Experimental section

Deposition of GNEC film: The GNEC films were deposited on the Si substrate by electron cyclotron resonance (ECR) sputtering system with low energy electron irradiation. The GNEC films were deposited on the Si substrate by using the electron cyclotron resonance (ECR) sputtering system. The Si substrate was cleaned in acetone and ethanol bath successively by ultrasonic waves. Before film deposition, the vacuum chamber was pumped down to 8×10^{-5} Pa and the argon was inflated to keep the working pressure with 1×10^{-1} Pa. A bias voltage of −500 V was applied to the carbon target for attracting the sputtering ions. The substrate was applied with a positive bias to form the electron irradiation. To our best research, the high edge density of graphene nanosheet was fabricated by setting the substrate bias 40 V.

Fabrication of GNEC mask: The GNEC mask was fabricated by the ultrasonic extrusion method. Electric carving device (JINTIAN MCD-50) with 11000/min high-frequency varication was used for breaking the GNEC film from the Si substrate. The ultrasonic-extrusion system (RAETTS) was used to embed GNEC nanostructure in smooth fibers. The extrusion time is 10 seconds with the ultrasonic frequency of 40 kHz and the working power of 600W. (See **Fig. S4** for detail information)

Characterization of the GNEC mask: SEM: the microstructures of the fibers were observed by scanning electron microscopy (SEM, FEI, Scios). ***TEM:*** the nanostructures of the carbon films were observed by transmission electron microscopy (TEM, FEI, Titan Cubed Themis G2 300). ***Water contact angle:*** the static contact angle (CA) of the sample surface was measured by the drop method using deionized water with a volume of 5 μL. In this work, all contact angle measurements were carried out in the same environment. The test instrument was a DSA 100S drop shape analyzer manufactured by KRUSS. Three different positions were measured on each sample surface, and the average value was reported as the final data. ***Raman:*** the Raman spectra were obtained with a Horiba HR800 Evolution system under the excitation laser wavelength of 532 nm. ***Optical absorption:*** the optical absorption spectrum was measured by a Solar cell quantum efficiency testing system (ZOLIX, SCS100). ***Solar illumination:*** the light source is acquired with the USHIO EKE 21V (150W) illuminating lamp, the light intensity can be adjusted by setting the input voltage (0 to 21V). ***Temperature mapping:*** the surface temperatures of the samples were measured by a FOTRIC 368T infrared camera. The filtration efficiency was measure by filter material performance tester (PALAS, PMFT-1000).

1 Electron cyclotron resonance (ECR) sputtering system

Figure S1 Electron cyclotron resonance (ECR) sputtering system.

Address correspondence to zh0005xi@szu.edu.cn

The GNEC films were fabricated by using an electron cyclotron resonance (ECR) plasma sputtering system. With the assistant of the low-energy electrons, graphene nanosheets embedded in amorphous carbon grow perpendicularly to the substrate. The atomic model of three-layer graphene sheets indicates the GNs embedded in amorphous carbon. A 500W-power microwave was delivered into the vacuum chamber to generate the plasma at the argon pressure of 4×10^{-2} Pa. The mirror confinement magnetic field was applied to enhance the plasma density. A negatively biased glassy carbon target was sputtered by Ar^{+} ions to generate carbon species towards the substrate. The thickness was controlled by deposition time. The deposition time of 30 min was adopted in this work and the thickness is ~70 nm. A positive deposited voltage (V_{dep}) was applied to the substrate for attracting electrons. With the assistant of the low-energy electrons, graphene nanosheets embedded in amorphous carbon grow perpendicularly to the substrate. The electron energy was modulated by V_{dep} which affects the size and number of GNs. We prepared films under V_{dep}=20 V, 40 V, 60 V and 80 V.

2 FIB processing to observe the cross-section of GNEC film

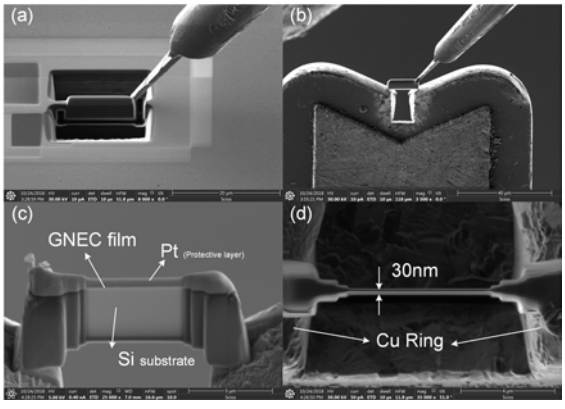

Figure S2 SEM images of (a) the origin cross-section sample, (b) the transferring cross-section sample. (c) the cross-section sample fabricated by using FIB, and sample located on a copper ring in preparation for TEM observation. (d) Top view of the cross-section, the thickness was thinned to 30 nm by ion irradiation.

The cross-section sample of 40 V GNEC film on the substrate was prepared by focused ion beam (FIB) etching. The protective layer is a layer of platinum having a thickness of 2 μm deposited on the surface of the sample by an auxiliary gas injection system associated with a FIB-SEM analysis system prior to FIB etching process. The lateral thickness of the cross-section sample was etched under 100 nm. As shown in the SEM image in **Fig. S2**, we prepare a cross-section sample with a thickness of about 30 nm, which is more conducive to our observation of the vertical growth structure of GNs under TEM. From the transmission electron microscopy (TEM) image of the cross-section sample, GNs grew vertically on the silicon substrate with a vertical thickness of ~70 nm.

3 TEM images to determine the graphene nanosheets (GNs) boundary

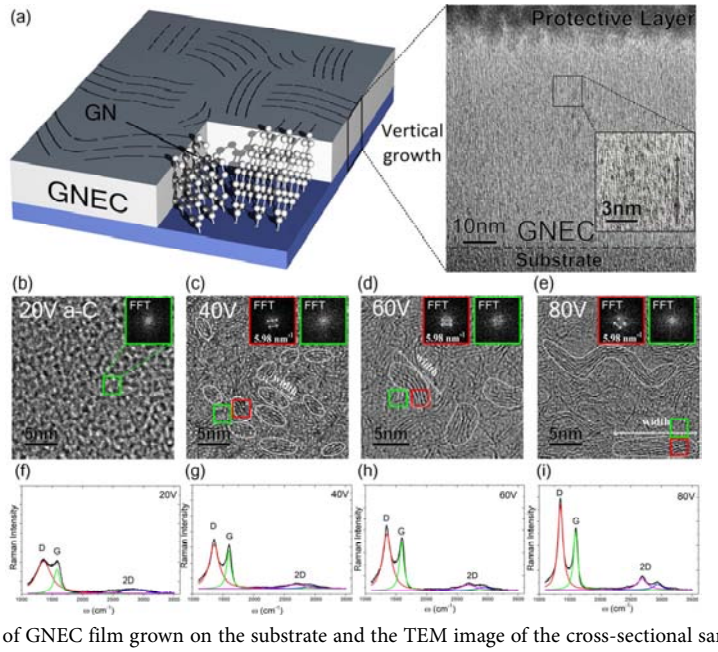

Figure S3 (a) Schematic diagram of GNEC film grown on the substrate and the TEM image of the cross-sectional sample prepared by FIB. Inset in the schematic diagram shows standing structured graphene nanosheets (GN) grown vertically on the Si substrate. High-resolution TEM plan-view images of GNEC films deposited at V_{dep} of (b) 20 V, (c) 40 V, (d) 60 V, and (e) 80 V. As the V_{dep} increases, GNs grow in width (as marked by white lines) among amorphous carbon film. Insets are the FFT images of the selected region (green and red squares). Raman Spectra of GNEC Films with V_{dep} of (f) 20 V, (g) 40 V, (h) 60 V, and (i) 80 V.

Fig. S3b-e shows the plan-view TEM images of films deposited at V_{dep} = 20V, 40V, 60V and 80 V. The energy of electrons was modulated by V_{dep} and calculated by e(V_{dep}-V_{plasma}), where V_{plasma} is the plasma potential measured as 10V. Red and green squares mark the regions inside and outside GN, as well as their fast Fourier transformation (FFT) images. FFT images show that inside the GN, two Laue spots appear corresponding to $(0001)^*$ facet of multilayer graphene. The reciprocal lattice distance $d^*_{(0001)}$ = 5.98/2 nm^{-1}=2.99 nm^{-1}, and the interplanar distance d = 1/2.99 nm = 0.334 nm, in accord with the (0001) facet distance of multilayer graphene. As the V_{dep} increases, irradiation electrons get higher energies to induce the growth of GNs. At V_{dep} = 20 V, the film is amorphous structure (a-C film) and contains a few GNs. At V_{dep} = 40 V, small-width GNs (≈ 3 nm) distribute randomly and densely among the film. At V_{dep} = 60 and 80 V, GN width grows to 7 and 15 nm on average. The crystallization of GNs enhanced by V_{dep} is verified by Raman spectra (**Fig. S3f-i**). At V_{dep} = 20V, the a-C film shows vague D and G peaks and no 2D band is observed. Above V_{dep} = 20V, the clear-shaped D band representing the long range ordered structure with sp^2 hybridization in amorphous structure. The intensity ratio of D peak over G peak (I_D/I_G) increases from 1.02 to 2.36 as the V_{dep} increases from 20 V to 80 V, indicating the increase of crystallization. Different from perfect graphene, in amorphous carbon film, D peak strength is proportional to the probability of finding a six-member ring, indicating ordering. In order to obtain the maximum edge density, the deposition voltage of 40 V for our considerations.

4 The schematic of ultrasonic system generator

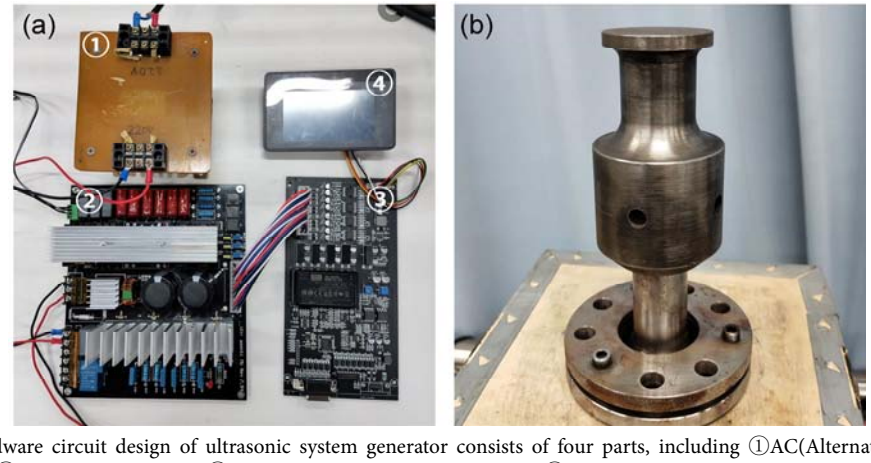

Figure S4 (a) The hardware circuit design of ultrasonic system generator consists of four parts, including ①AC(Alternating Current)--DC(Direct Current) transformer; ②The power amplifier; ③Control system for power amplifier; ④Touching screen. (b) Ultrasonic transducer.

The ultrasonic wave is used to convert high-frequency electrical energy into mechanical vibration through a transducer. As shown in Fig. S4, the current transformer is used for changing the AC to DC. The power amplifier converts direct current to high frequency high voltage. The output voltage can be controlled by a control system. People can input the expected output voltage signal by touching the screen. Finally, using an ultrasonic transducer, high frequency and high voltage can output ultrasonic wave stably.

Advantage of Generator: All-digital integrated circuit, using high-performance anti-interference processor, while reducing the number of components, simplifying the hardware structure, and increasing the voltage regulator function to improve the reliability and stability of the system. The application of IGBT power module and the structure of other excited oscillation circuits make the output power more than 1.5 times of the traditional self-excited circuit. Using amplitude stepless adjustment, The setting range of amplitude is 10% ~ 100%.

5 Ultrasonic extrusion process of GNEC mask

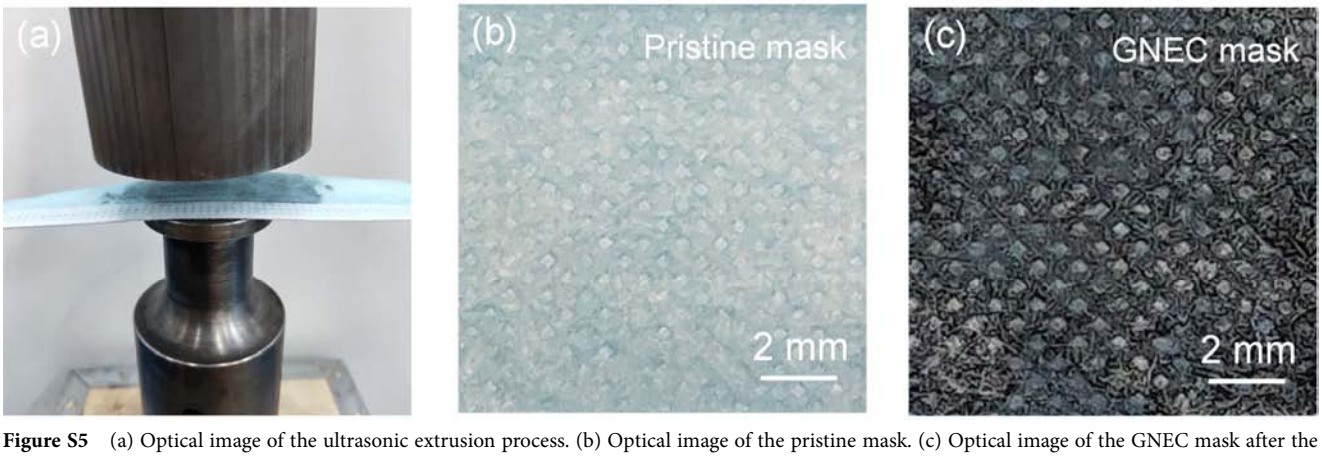

Figure S5 (a) Optical image of the ultrasonic extrusion process. (b) Optical image of the pristine mask. (c) Optical image of the GNEC mask after the ultrasonic extrusion process.

6 The rolling angle of GNEC mask surface

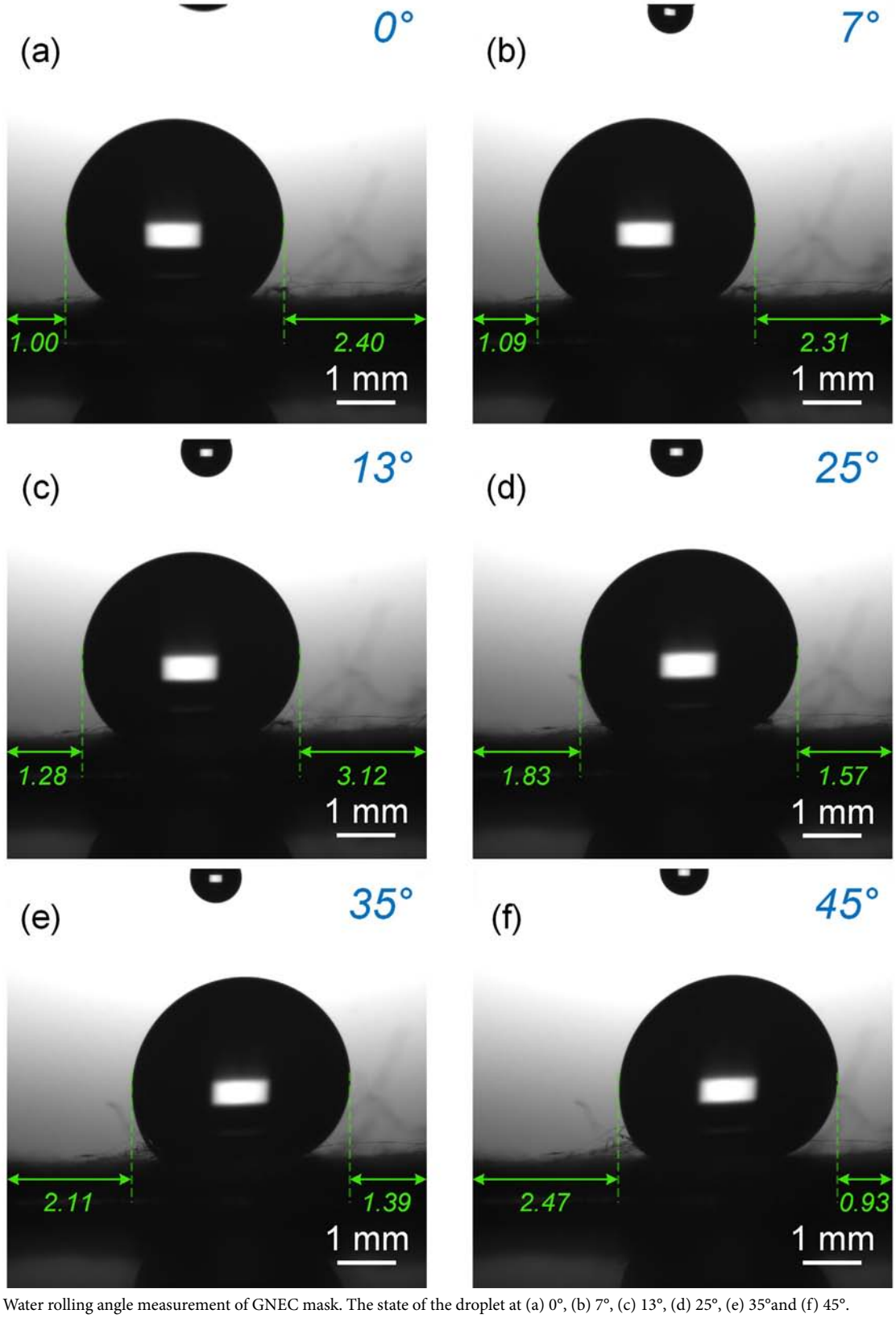

Figure S6 Water rolling angle measurement of GNEC mask. The state of the droplet at (a) 0°, (b) 7°, (c) 13°, (d) 25°, (e) 35°and (f) 45°.

The water contact angle measure platform has a tilt of 90° feature. We measure the water rolling angle by the tilt platform, to simulate the normal use of masks. The tilt angle of the measurement platform is 0° to 90° (tilt speed: 0.5°/s). **Fig. S6** shows the water rolling process of the GNEC mask. At a small inclined angle (7°C) of the platform, the droplets perceptibly roll on the mask surface.

7 The water contact angle of GNEC mask after solar illumination.

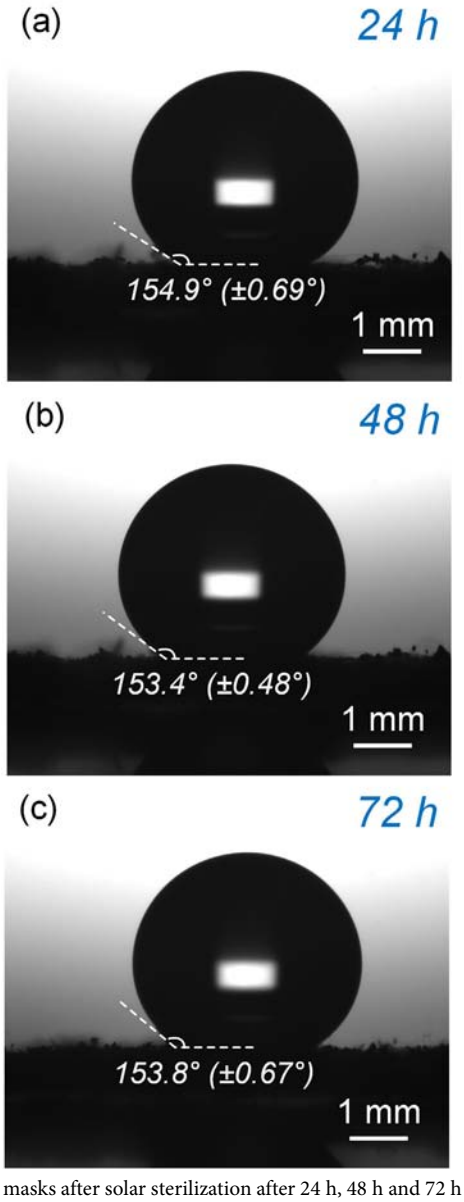

Figure S7 The water contact angle of the GNEC masks after solar sterilization after 24 h, 48 h and 72 h with solar illumination (at 15V input voltage).

Under the long period of solar illumination, the surface hydrophobic feature of the GNEC mask with no declining performances, suggested that the GNEC mask is reusable.

8 Temperature mapping of GNEC mask after 48h illumination.

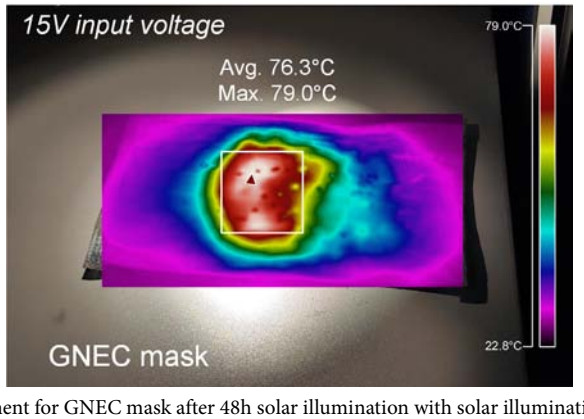

Figure S8 Surface temperature measurement for GNEC mask after 48h solar illumination with solar illumination at (15V input voltage).

9 Air resistance and filter efficiency of GNEC mask after solar illumination.

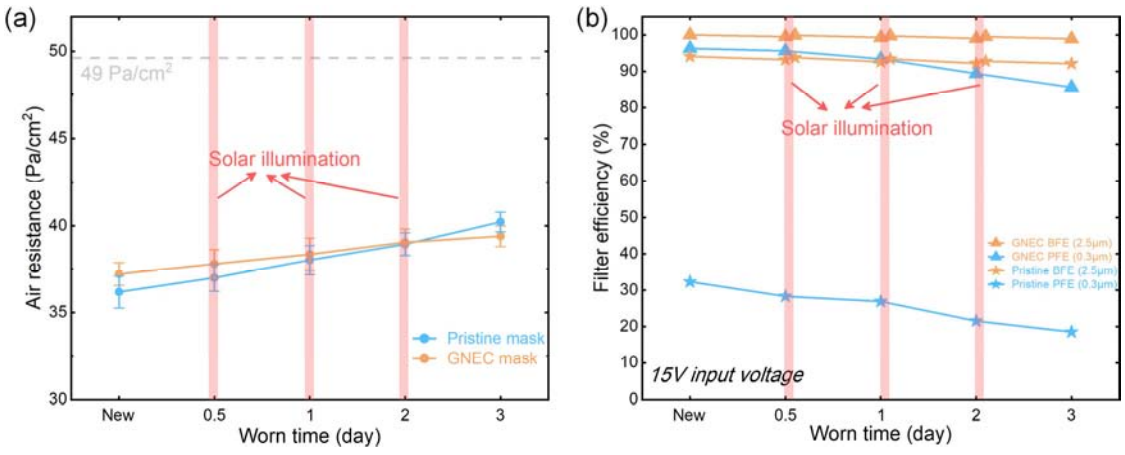

Figure S9 (a) The air resistance of pristine masks and GNEC masks. (b) The cycling experiment of filter efficiency under solar illumination.